Journal of Catalysis **185,** 237–251 (1999)
Article ID jcat.1999.2522, available online at http://www.idealibrary.com on IDEAL®

Temperature Programmed Desorption of Oxygen from Ag Films Interfaced with Y_2O_3-Doped ZrO_2

D. Tsiplakides and C. G. Vayenas

Department of Chemical Engineering, University of Patras, Patras GR-26500, Greece

Received November 9, 1998; revised April 12, 1999; accepted April 12, 1999

The origin of the effect of nonfaradaic electrochemical modification of catalytic activity (NEMCA) or electrochemical promotion was investigated via temperature-programmed desorption of oxygen from polycrystalline Ag films deposited on 8 mol% Y_2O_3-stabilized ZrO_2 (YSZ), an O^{2-} conductor, under high-vacuum conditions and temperatures of 200 to 400°C. Oxygen was adsorbed both via the gas phase and electrochemically, as O^{2-}, via electrical current application between the Ag catalyst film and a Au counterelectrode. Gaseous oxygen adsorption gives a single adsorption state ($T_p \approx 290$–335°C) at low adsorption temperatures with subsurface oxygen ($T_p \approx 500$°C) also forming for higher adsorption temperatures ($T > 350$°C). Electrochemical or mixed gaseous–electrochemical adsorption was found to cause significant oxygen backspillover from the YSZ solid electrolyte onto the Ag surface and the creation of two distinct oxygen adsorption states, i.e., a strongly bonded ionic state and a weakly bonded state. The strongly bonded state ($T_p \approx 380$–400°C) is identical to the one formed via electrochemical adsorption. The weakly bonded state ($T_p \approx 320$–340°C) desorbs at temperatures similar with the gaseous adsorption state. The creation of these two states is also manifest by high temperature cyclic voltammetry. Mixed adsorption leads to much higher oxygen coverages than gaseous adsorption. The binding strength of the weakly bonded oxygen state was investigated as a function of applied potential. It was found that the binding energy of adsorbed oxygen decreases linearly with increasing catalyst potential and work function. The results suggest that, similarly to the case of Pt, the non-Faradaic rate enhancement observed in NEMCA studies of catalytic oxidations on Ag/YSZ is due to the creation of two adsorption states, of which the weakly bonded one is highly reactive while the strongly bonded one acts as a sacrificial promoter. The fact that, unlike Pt, the Tp of the weakly bonded state is not lower than that of oxygen formed via gaseous adsorption can account for the less pronounced NEMCA behavior of Ag vs Pt catalysts.

INTRODUCTION

The adsorption of oxygen on silver has been the subject of numerous studies for many years. The interest for this system arises mainly from the importance of silver as a catalyst for the partial oxidation of ethylene to ethylene oxide (1–4). The interaction of O_2 with Ag surfaces is also of great importance for the understanding of the dynamics of molecule–surface interactions, as this system can be regarded as a prototype for a three-well interaction potential (5–8). Therefore, numerous surface science techniques have been used to study the adsorption of O_2 on Ag (9–51) along with theoretical studies. The studies have been carried out on single crystals (9–34), polycrystalline samples (35–47), and promoted Ag catalysts (48–50) in the temperature range from –173 to 600°C from UHV to atmospheric pressure conditions. Arakawa *et al.* (51) were first to study the properties of Ag films deposited on oxygen-ion-conducting solid electrolytes (ZrO_2–CaO 11 mol%) in a cell of the type P_{O_2}, Ag | ZrO_2–CaO | Ag, P_{O_2}.

The basic results from the studies on Ag single crystals are the following. On Ag(110) three different states of chemisorbed oxygen have been identified (9–26). At low temperatures, below −123°C, a molecularly chemisorbed state, $O_{2,a}$, with the O–O bond parallel to surface, predominates. This species, thought to be a peroxo-like one, has a desorption activation energy of 46 kJ mol^{-1}. At about −83°C, this species partially desorbs as O_2 or dissociates into two oxygen adatoms, O_a. These adatoms, which can penetrate the surface to form an unreactive subsurface species, O_b, are stable on the surface up to 307°C, where they desorb. The activation energy for the desorption has been determined to 142–188 kJ mol^{-1}. The so-called atomic "subsurface oxygen," described by Backx *et al.* (16, 17), does not desorb at temperatures below 447°C. In a few studies also the formation of a silver oxide phase Ag_2O has been observed even at low pressures. Quite similar oxygen chemisorption states have been reported for Ag(111) (27–34), namely a molecularly chemisorbed species desorbing at about −58°C, a dissosiative chemisorbed species, which desorbs at ∼307°C, leading in subsurface sites, desorbing at ∼427°C. These states are populated with much lower sticking probability on Ag(111) than on Ag(110). For example, the dissociative sticking coefficient is of the order of 10^{-6} for Ag(111) while a value of 2×10^{-4} for Ag(110) has been reported at 217°C (27).

The role of subsurface oxygen in catalysis, and especially for the case of ethylene epoxidation on Ag, has been studied

0021-9517/99 $30.00

for years (52). The main conclusions are the following:

1. The chemisorption bond strength of oxygen decreases due to the presence of subsurface oxygen.
2. Subsurface oxygen pushes part of the adsorbed O($2p$) levels to higher energies. As a consequence, the adsorbed oxygen–ethylene strongly anti-bonding levels rise above the Fermi level. Therefore, the ethylene–oxygen interaction, which is repulsive in the absence of subsurface oxygen, becomes attractive when subsurface oxygen is present.
3. As a consequence of these two effects, the barrier for reaction to epoxide disappears. Subsurface oxygen seems to be necessary for adsorbed oxygen to react to epoxide.

Recently, it has been found that the catalytic activity and selectivity of metals interfaced with solid electrolytes can be altered dramatically and reversibly by application of an electrical current or potential between the metal catalyst film and a second metal film (counterelectrode) also deposited on the solid electrolyte (53–56). The increase in catalytic rate can be several, typically two to five, orders of magnitude higher than that anticipated from Faraday's Law (53–56). Thus electrochemical O^{2-} supply to polycrystalline Ag catalyst films deposited on Y_2O_3-stabilized ZrO_2 (YSZ) and exposed to ethylene–oxygen mixtures causes a catalytic oxidation rate increase, Δr, which is typically 10^2 times higher than the rate, $I/2F$, of O^{2-} supply to the catalyst (56). Therefore, each O^{2-} supplied to the catalyst causes 10^2 chemisorbed oxygen atoms to react with ethylene and form CO_2 and C_2H_4O. This new phenomenon of electrochemical promotion, also known in the literature as nonfaradaic electrochemical modification of catalytic activity (NEMCA effect), is of considerable theoretical and potentially practical importance.

During the past 10 years the NEMCA effect has been studied for over 50 catalytic reactions on Pt, Rh, Pd, Ag, Ni, Au, IrO_2, and RuO_2 catalyst films deposited on O^{2-}, F^-, Na^+, and H^+ conducting solid electrolytes (53–64) as well as mixed electronic–ionic conductors, such as TiO_2 (65), and aqueous alkaline solutions (66). The importance of NEMCA in catalysis (67), surface science (68), and electrochemistry (69) has been discussed and work prior to 1996 has been reviewed (55, 56). Despite the large number of different ionic conductors which have been used to induce and study electrochemical promotion most of the work in this area has utilized YSZ as the solid electrolyte.

Silver polycrystalline films supported on YSZ have been used in NEMCA studies to enhance the rate of CO oxidation (70), ethylene and propylene epoxidation (71–75), and methanol dehydrogenation and decomposition (76), in the temperature range of 280–400°C. The oxidative coupling of CH_4 has also been investigated at higher temperatures (650–850°C) but in this case the behavior was faradaic (77). In the case of C_2H_4 and C_3H_6 epoxidation and OCM reaction, modifications on product selectivity via the NEMCA effect have also been observed under electrochemical promotion conditions. The enhancement factor or Faradaic efficiency, Λ, defined as

$$\Lambda = \Delta r/(I/2F), \qquad [1]$$

ranges from -1.2 to 300 for the case of silver catalyst films. Both electrophobic ($\Lambda > 1$) and electrophilic ($\Lambda < -1$) behavior has been noticed.

The rate enhancement ratio, ρ, defined as

$$\rho = r/r_o, \qquad [2]$$

where r is the electrochemically promoted catalytic rate and r_o is the open-circuit (unpromoted) catalytic rate value, reaches a maximum value of 30 for CH_4 oxidation (77), but is typically between 0.03 and 3 for ethylene epoxidation (74, 75).

The origin of electrochemical promotion has been investigated using a variety of techniques including STM (78), XPS (79), SERS (80, 81), TPD (72, 83), UPS (84), and the Kelvin probe method (85–87). A key step in the elucidation of the origin of NEMCA was the experimental discovery (54, 84) and theoretical confirmation (53) that solid electrolyte cells with metal electrodes are both work function probes and work function controllers for the gas-exposed surfaces of their electrodes. Both Kelvin probe (85–87) and UPS (84) measurements have shown that

$$eV^o_{WR} = e\Phi_W - e\Phi_R \qquad [3]$$

$$e\Delta V_{WR} = \Delta(e\Phi_W), \qquad [4]$$

where V_{WR} is the catalyst-working (W) electrode potential, V^o_{WR} stands for the open-circuit potential, and $e\Phi_W$ and $e\Phi_R$ are the average work functions of the working and reference electrodes, respectively. Equations [3] and [4] are also consistent with the spillover/backspillover ion mechanism proposed to explain the electrochemical promotion effect. The change in work function upon application of an external potential ΔV_{WR} is due to the migration of ionic species on the gas-exposed catalyst-electrode surface.

In the case of NEMCA with O^{2-}-conducting solid electrolytes, like YSZ, upon positive current application oxygen ions are pumped through the YSZ to the silver catalyst-working electrode. These ions can follow two possible pathways. Oxygen ions can dispose of their charge at the three-phase boundaries and form spillover dipoles which can spread over the catalyst surface.

In addition to this charge transfer (electrocatalytic) mechanism, there is another possibility due to the finite solubility of oxygen in Ag: oxygen ions go through the Ag as dissolved oxygen and then emerge at the catalyst surface, giving rise to the formation of covalently bonded chemisorbed oxygen. Both oxygen species cause an increase on catalyst work function. XPS has shown that, under

conditions of electrochemical O^{2-} supply to Ag catalyst-electrodes deposited on YSZ at 400°C, the O1*s* binding energy of spillover dipoles is 529.2 eV (51). This is lower than the value of 529.8 ± 0.3 eV for normally chemisorbed atomic oxygen (32) which can coexist on the Ag surface (51). The lower value of the O1*s* binding energy of the spillover oxygen species suggests a stronger ionic character in its binding with the Ag surface than normally chemisorbed atomic oxygen. Nevertheless, the through-the-Ag pathway which results in an increase in the coverage of the more covalently bonded oxygen must also contribute to the $e\Phi$ increase. Thus the role of the through-the-Ag pathway is not simply to provide more oxygen on the surface but also to weaken the Ag–atomic oxygen bond, via increasing $e\Phi$, along with the $e\Phi$ increase caused by the more ionically bonded spillover atomic oxygen species (74).

The technique of isothermal surface titration (56, 74), described below, has also been used to investigate the chemisorptive properties of porous Ag films deposited on YSZ in a solid electrolyte cell (74). It was found that the chemisorptive properties of Ag can be influenced in a pronounced and reversible manner upon polarizing electrochemically the metal–solid electrolyte interface. Decreasing catalyst potential and work function was found to strengthen significantly the Ag–atomic oxygen chemisorptive bond.

In a recent paper (82) we have presented a detailed TPD investigation of oxygen adsorption on Pt films interfaced with YSZ, which provides a direct explanation for electrochemical promotion effect in Pt/YSZ systems. In the present work we present a detailed TPD investigation of oxygen adsorption on Ag deposited on YSZ and analyze the effect of applied potential on the binding states of adsorbed oxygen. The investigation is supplemented by cyclic voltammetric data and can be used to rationalize the electrochemical promotion effect in Ag/YSZ systems.

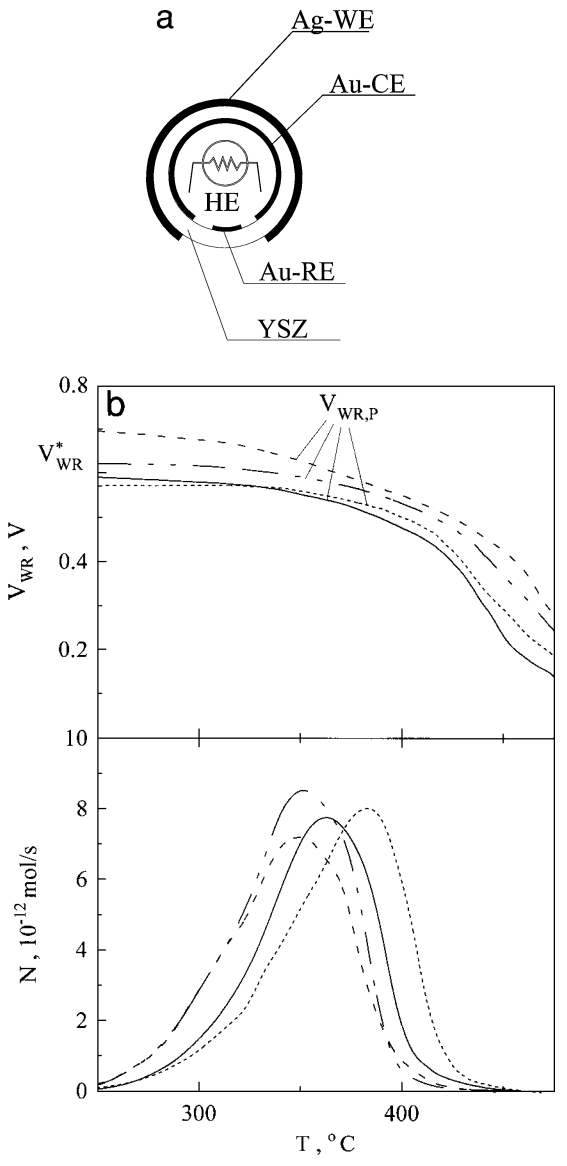

FIG. 1. (a) Schematic cross section of the YSZ tube showing the location of the Ag film catalyst-working electrode (WE), the Au counter (CE), the reference (RE) electrodes, and the heating element (HE). (b) Thermal desorption spectra (bottom) and corresponding catalyst potential variation (top) after electrochemical O^{2-} supply at 260–320°C at various polarizations V^*_{WR}, resulting in constant initial oxygen coverage. V^*_{WR} is the catalyst potential at the beginning of the TPD run and $V_{WR,P}$ is the catalyst potential at the peak desorption temperature.

EXPERIMENTAL

1. Catalyst Preparation and Characterization

The Ag film was deposited in the form of a half-ring on the outer surface of a tubular YSZ (ZrO_2–Y_2O_3 8 mol%) specimen (Fig. 1a). The electrolyte tube had an outer diameter of 19 mm, a thickness of 2 mm, and a length of 50 mm. On the inner surface of the tube a counterelectrode and a reference Au electrode were deposited with the former one facing the silver working electrode. Details on the preparation and characterization of the Ag and Au electrodes are given elsewhere (56, 71). Auger electron spectroscopic analysis of similarly deposited Ag films (71) has shown the absence of any significant surface impurities. In this way a three-electrode cell arrangement was constructed. The superficial surface area of the Ag film was 1.25 cm^2 and its true surface area was 285 cm^2. The latter was computed by the isothermal titration technique (56, 74), i.e., by measuring its reactive oxygen uptake ($N_O = 7.1 \times 10^{-7}$ mol of O) via oxygen titration with C_2H_4 at atmospheric pressure and 347°C as described in detail elsewhere (56).

A series of blank TPD experiments showed that the YSZ specimen and the Au electrodes did not desorb any measurable amount of oxygen. Thus all the TPD spectra reported here can safely be attributed to oxygen chemisorption from the Ag film only.

The catalyst was cleaned in the vacuum system. The "clean-up" procedure includes the treatment of the surface with oxygen from the gas phase or with electrochemically supplied oxygen from the solid electrolyte followed by temperature programmed desorption. This resulted in a gradual increase of the amount of oxygen desorbing after a fixed dose. At the end of the clean-up treatment a reproducible oxygen desorption spectrum was achieved. Furthermore, no CO signal was detected during TPD, which is a good indication for the absence of carbon on the surface.

2. Experimental Apparatus

The specimen was placed in an ultrahigh vacuum chamber, with base pressure of about 10^{-9} Torr after baking, where all the experiments were carried out. The vacuum chamber was equipped with a quadruple mass spectrometer (Balzers QMG 420) and a leak valve gas inlet system. The signal of the spectrometer was calibrated to give the desorption rate, dN/dt, in mol/s.

The sample was heated radiatively using an Osram xenon lamp located inside the YSZ tube. A type-K thermocouple attached on the Ag surface was used to measure the temperature. The temperature could be varied linearly at a heating rate as high as 2 K/s using a Eurotherm programmable temperature controller.

Constant currents between the Ag film and the Au counterelectrode (galvanostatic operation) or constant potentials between the Ag film and the Au reference electrode (potentiostatic operation) were applied by an AMEL 553 galvanostat–potentiostat. Furthermore, with this apparatus it was possible to monitor continuously the potential, V_{WR}, of the Ag film with respect to the Au-reference electrode under open circuit conditions.

By the use of Eq. [4], which relates the change in catalyst potential V_{WR} with the induced change in catalyst work function $e\Phi$, it was thus possible to monitor the change in the average work function of the polycrystalline Ag film during adsorption and desorption experiments. An AMEL 567 function generator was used, in conjuction with the galvanostat–potentiostat, for the cyclic voltammetric experiments.

3. Oxygen Adsorption

Three modes of oxygen adsorption on the Ag film were used at temperatures of 200–400°C:

1. Gaseous oxygen adsorption by exposure to P_{O_2} of the order of 10^{-6} Torr for various exposure times, t_{O_2}, corresponding to several kilolangmuirs ($1\ \text{kL} = 10^{-3}\ \text{Torr}\cdot\text{s}$). The O_2 gas was injected to the vacuum chamber through a leak valve.

2. Electrochemical oxygen supply at a rate $I/2F$ for various times, t_I, of positive current I application between the Ag film and the Au counterelectrode. In this case oxygen is locally depleted from the YSZ solid electrolyte in the vicinity of the Au counterelectrode without any loss in cell reversibility.

3. Mixed gas and electrochemical adsorption. In this mode the film was first exposed to $P_{O_2} = 6 \times 10^{-6}$ Torr for time t_{O_2}, followed by electrochemical supply of oxygen through the solid electrolyte for a time t_I.

After oxygen adsorption, the sample was cooled rapidly under open circuit, followed by a linear increase in temperature at a heating rate β(°C/s) again under open circuit in order to obtain the TPD spectra.

In order to determine the oxygen desorption activation energy, E_d, and its dependence on catalyst potential a series of low coverage TPD experiments was carried out. The exact experimental procedure was described in detail in a recent paper (82). Briefly, a constant positive current I was applied for a time t_I to supply oxygen to the catalyst at a rate $I/2F$ and to establish a small initial coverage θ_o on the Ag catalyst surface, kept constant within experimental error (~10%). This current application was performed at seven different temperatures, resulting in seven different induced catalyst potentials V^*_{WR} at the end of the time of current application, due to the effect of T on the exchange current I_o of the Ag–YSZ interface (56).

At the end of t_I the current was stopped, and the sample was cooled rapidly without any significant change in the open circuit potential V^*_{WR}. The sample temperature was then increased at a heating rate β, ranging from 0.4 to 2 K/s, to obtain the TPD spectra. We thus obtained 56 different peak desorption temperatures T_p ranging from 330 to 405°C and corresponding to different pairs of V^*_{WR} and β. These data were used to extract the activation energy of oxygen desorption E_d via the standard Redhead analysis as generalized by Falconer and Madix (88).

The above experimental procedure, regarding t_I and V^*_{WR}, was followed during all electrochemical and mixed adsorption experiments, including those with high initial oxygen coverage. Thus V^*_{WR} always refers to the catalyst potential value at the end of current application and thus also at the start of the TPD spectrum. As shown in Fig. 1b, which presents typical oxygen TPD spectra after electrochemical O^{2-} supply, leading to various V^*_{WR} values (with the corresponding I and t_I values chosen so that the initial oxygen coverage is nearly constant), the value of V_{WR} during the TPD spectrum deviates little (less than 80 mV) from the initially imposed V^*_{WR} value up to the peak desorption temperature T_p. Thus V^*_{WR} provides a very good, albeit of course approximate, measure of the catalyst–electrode potential during the initial steps of the desorption process and up to the peak desorption temperature. An alternative way of analyzing the data, which we also tried, is to relate the measured E_d values with the V_{WR} value, $V_{WR,P}$, at the peak desorption temperature T_p. As expected since V^*_{WR} and $V_{WR,P}$ differ by less than 80 mV, both methods lead to

the same qualitative conclusions regarding the dependence of E_d on catalyst potential V_{WR}.

RESULTS AND DISCUSSION

1. Gas Phase Adsorption

Figures 2a–2d show the oxygen thermal desorption spectra after exposure of the Ag film to oxygen for various times. The exposure times, expressed in kilolangmuirs, are shown in the figures. For the three lower adsorption temperatures, 250, 300, and 350°C, a single peak is obtained, attributed to the dissociatively chemisorbed oxygen species. It should be noted that in the temperature range of the present study only atomic species can exist on the surface, since the molecular species on Ag desorb or dissociate at temperatures below −50°C. For adsorption temperature 200 and 250°C the peak maximum appears at about 293°C, very close to the reported value of ∼307°C for Ag single crystals (27). When the adsorption temperature is raised to 300°C, the peak desorption, T_p, increases to ∼335°C.

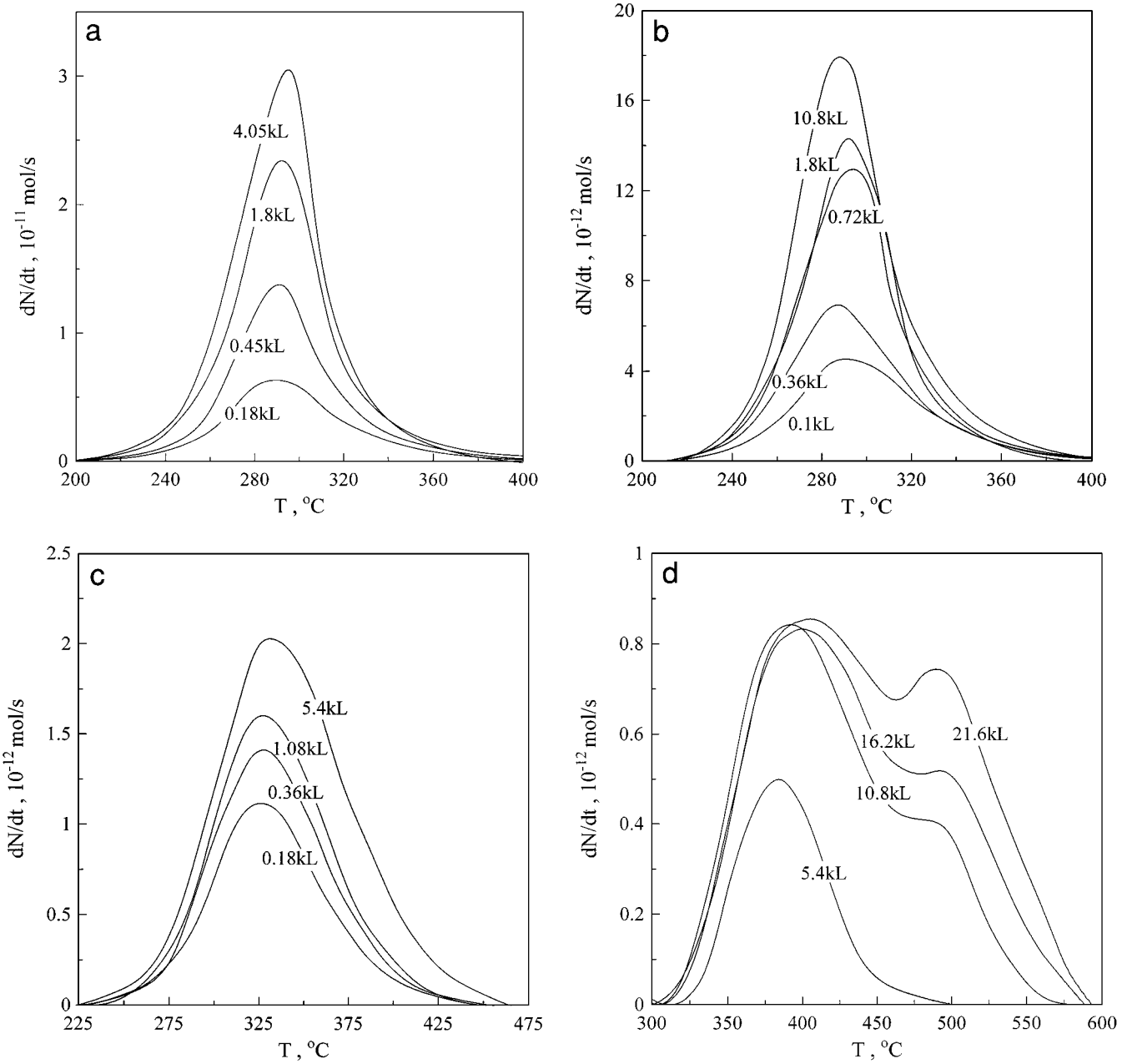

FIG. 2. (a–d) Oxygen thermal desorption spectra after gaseous oxygen dosing for various exposure times at (a) 200°C, $P_{O_2} = 1.5 \times 10^{-6}$ Torr, (b) 250°C, $P_{O_2} = 6 \times 10^{-6}$ Torr, (c) 300°C, $P_{O_2} = 6 \times 10^{-6}$ Torr, and (d) 350°C, $P_{O_2} = 6 \times 10^{-6}$ Torr. Oxygen exposure is expressed in kilolangmuirs (1 kL = 10^{-3} Torr · s). Desorption was performed with linear heating rate, $\beta = 1$ K/s.

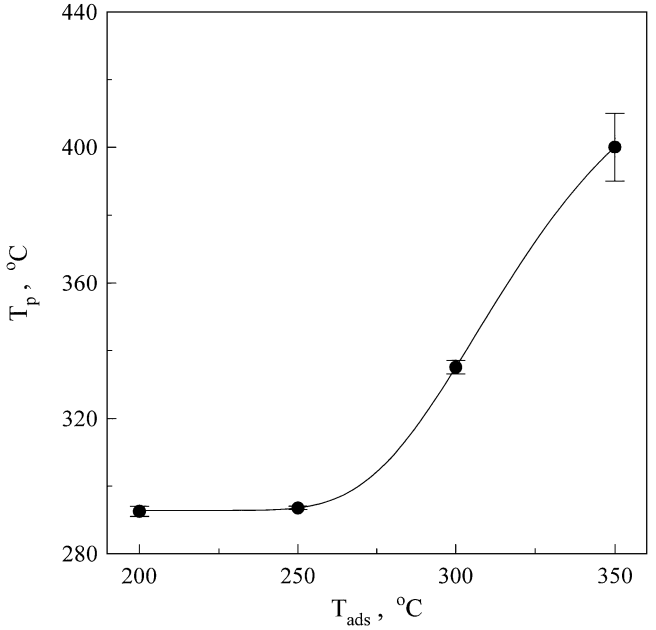

FIG. 3. Peak desorption temperature as a function of adsorption temperature as extracted from Figs. 2a–2d.

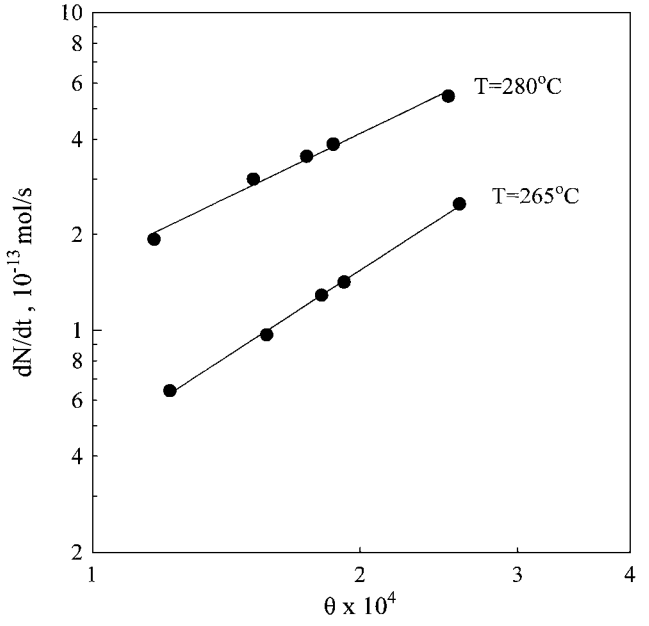

FIG. 4. Desorption rate isotherms obtained from thermal desorption spectra of Fig. 2a, indicating first-order desorption rate.

Furthermore, the peaks are wider compared to those at lower adsorption temperatures. This shift of the maximum, by about 40°C, in conjunction with the broadening of the peaks is an indication for the formation of small amount of subsurface oxygen. The existence of the subsurface species is very clear when the adsorption temperature is 350°C (Fig. 2d). In this case two peaks are present for long exposures. The second peak corresponds to subsurface oxygen desorbing at 490°C (in Ag(110) the subsurface oxygen does not desorb at temperatures below 450°C (23)). It is obvious that the large amount of this species at high temperature is due to the faster diffusion from the surface to the bulk. Figure 3 depicts the effect of adsorption temperature, T_{ads}, on the desorption temperature, T_p, showing a sharp increase in T_p when T_{ads} is higher than $\sim$275°C, i.e., the temperature which coincides with the onset of subsurface oxygen formation.

From the desorption curves of Fig. 2a, corresponding to different initial coverage, a plot of ln N versus ln θ at constant temperature can be made (Fig. 4). Following the standard Falconer–Madix analysis (89) it follows that this desorption rate isotherm should be a straight line with slope n, where n is the order of desorption, assuming that the activation energy is independent of coverage. Repeating this procedure for two temperatures, we obtain two desorption isotherms with slopes between 0.93 and 1, strongly indicating first-order desorption.

Under all experimental conditions used for gas phase adsorption, a shift of desorption rate maximum due to different initial coverage has not been observed. This is in agreement with previous TPD studies of oxygen on Ag (32) and shows the absence of strong lateral interactions between the oxygen adatoms. This can be explained from the fact that the oxygen coverages resulting from gaseous adsorption are, at least in the present study, very small due to the high adsorption temperatures.

The adsorption profiles for oxygen are shown in Fig. 5 for the above adsorption temperatures. The oxygen coverages

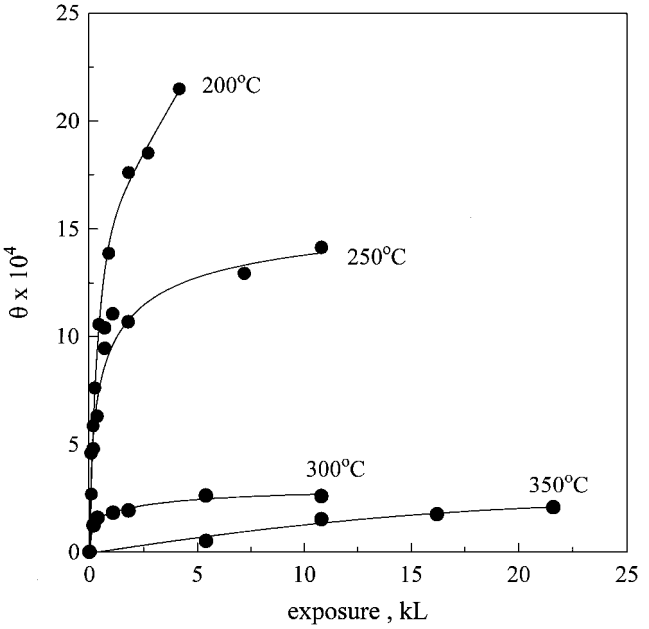

FIG. 5. Adsorption profiles for oxygen adsorption at 200, 250, 300, and 350°C, corresponding to the thermal desorption spectra of Figs. 2a–2d.

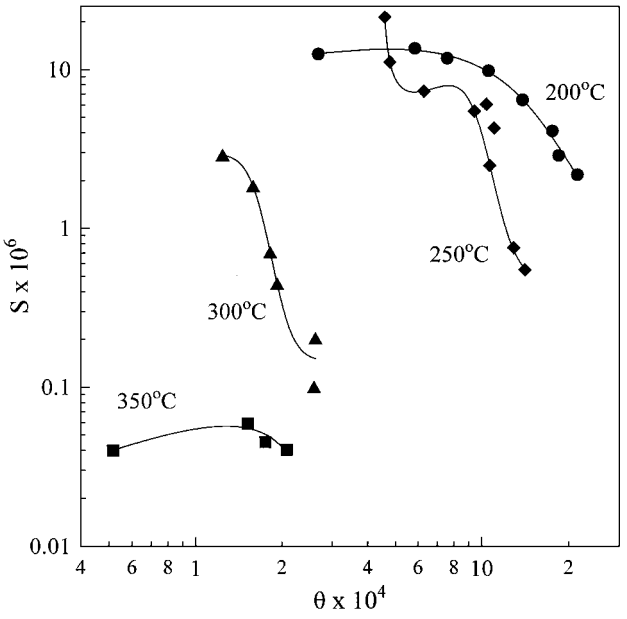

FIG. 6. Integrated sticking coefficient as a function of oxygen coverage during adsorption at 200, 250, 300, and 350°C.

have been computed from the corresponding TPD spectra by integration and using the maximum reactive oxygen uptake $N_O = 7.1 \times 10^{-7}$ mol of O measured via titration of adsorbed oxygen with C_2H_4 at atmospheric pressure (56, 74).

The sticking coefficient for gas phase adsorption, S (see Fig. 6), is defined as the ratio of the adsorbed oxygen molecules (estimated from integration of the thermal desorption spectra) over the total oxygen molecules that collide with the surface, i.e., $(P_{O_2}/2\pi MRT_g)^{1/2} \cdot A \cdot t_{O_2}$, where P_{O_2} is the oxygen partial pressure in Torr, M is the molecular weight of O_2, R is the gas constant, T_g is the gas temperature, A is the total surface of the catalyst film, and t_{O_2} is the oxygen exposure time. For gas phase adsorption the integrated sticking coefficient is plotted against oxygen coverage. The sticking coefficient varies from 3×10^{-8} to 1.5×10^{-5} strongly depending on coverage and adsorption temperature. As expected S drops with increasing coverage and adsorption temperature. In all cases the value of S is in the order of magnitude of the values reported for single crystals. By comparison with the results of Campbell at 217°C (27) the polycrystalline Ag film surface appears to consist mostly of the (111) plane. It is worth noting that although the coverages are quite small, one observes a pronounced decrease in sticking coefficient with increasing oxygen coverage.

As already mentioned, by the use of the Au reference electrode it was possible to follow continuously the change of the average work function of the Ag film during adsorption and desorption procedure. Figure 7 depicts the growth of $\Delta(e\Phi)$ with exposure at various temperatures during oxygen adsorption from the gas phase. Due to the linearity of $\Delta(e\Phi)$ with coverage (9), $\Delta(e\Phi)$ can be used as a coverage indicator. The work function of Ag could be increased by up to 0.7 V when saturation was achieved. These results are in accordance with the observations of Engelhardt and Menzel (9) on Ag(110). It should be noted that for the lowest adsorption temperature, 200°C, it was not possible to measure the changes in work function with the present instrumentation. The reason is that in order to measure $\Delta(e\Phi)$ one has to monitor V_{WR} under open circuit conditions, which requires significant ionic conductivity of the solid electrolyte; this is not the case in YSZ at this low temperature.

By using the modified Redhead analysis by Falconer and Madix (88), the activation energy for desorption is estimated (Fig. 8). From the slope of the Redhead lines $\ln(\beta/T_p^2)$ vs $1/T_p$ we obtain a value 130–140 kJ/mol for the desorption activation energy, which is in good agreement with the literature (9, 25–28, 32, 50).

2. *Electrochemical Adsorption*

Figures 9–11 show oxygen thermal desorption spectra obtained after electrochemical O^{2-} supply to the Ag film through the solid electrolyte for three temperatures and various currents, I, and current application times, t_I. In all cases the coverages achieved are much higher than those obtained with gas phase adsorption. This is also accompanied with much higher sticking probabilities, as shown below. This seems to be a general observation since the same behavior was observed for Pt (82, 83) and Au (90). In

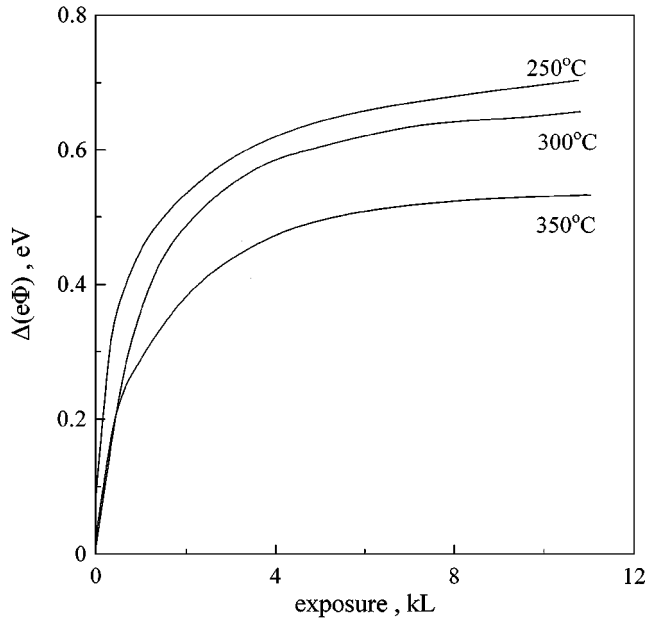

FIG. 7. Work function change versus exposure on oxygen at various adsorption temperatures and an O_2 pressure of 6×10^{-6} Torr.

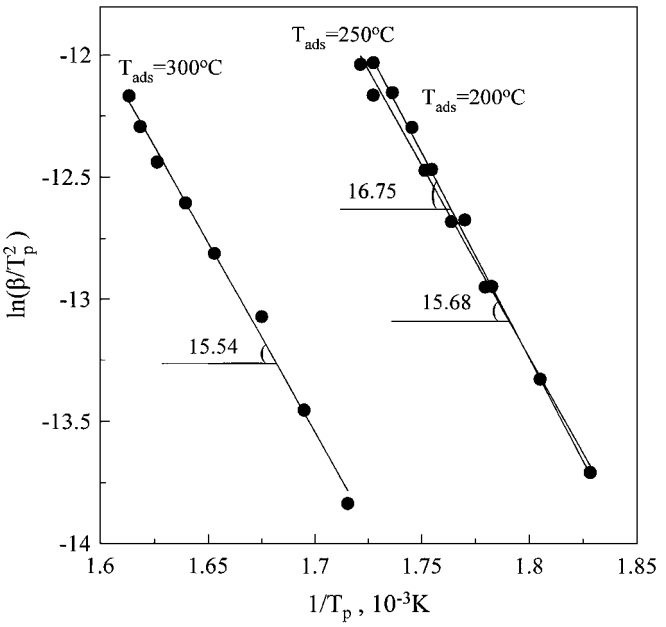

FIG. 8. Log(β/T_p^2) as a function of $1/T_p$ for three adsorption temperatures, for the adsorption of O_2 from the gas phase with a pressure of 6×10^{-6} Torr. The slope of each curve is equal to E_d/R according to the modified Redhead analysis of Madix and Falconer (88).

contrast with the case of gas phase adsorption, one observes a shift of the rate maximum to higher temperatures as one increases the current application time or, equivalently, the oxygen coverage. This is explained from the much higher coverages achieved by electrochemical adsorption. Almost all desorption peaks are wider than those corresponding to gas phase adsorption, suggesting the coexistence of a second oxygen species. This becomes more evident for the case of $T_{ads} = 350°C$ and $I = +10\,\mu A$ (Fig. 10b). Under these adsorption conditions one sees clearly the gradual growth of a second high temperature peak with increasing current application time. This peak appears at lower temperature ($\sim$460°C) than the normal subsurface oxygen. At the same time the first peak is at about the same temperature as the corresponding peaks from gas phase adsorption. The existence of two peaks is even suggested in Fig. 12a, where some TPD spectra with practically the same (low) initial coverage are presented. They correspond to the same adsorption temperature and different currents and current application times. For low current only one peak is obtained at high temperatures, while at higher currents a second peak at lower temperature appears. Finally, in Fig. 12b the effect of adsorption temperature on oxygen adsorption is presented for the case of electrochemical oxygen supply. Again we observe a shift of the maximum to higher temperatures as we increase the adsorption temperature with a concomitant decrease in V^*_{WR}. In the insets of Figs. 12a and 12b the effect of potential, V^*_{WR}, on peak temperature is presented. In both cases, T_p decreases significantly with increasing preapplied potential.

The sticking coefficient in electrochemical adsorption can be defined as the ratio of adsorbed oxygen molecules, calculated from integration of the TPD spectra, over the total number of oxygen atoms that are supplied through the solid electrolyte ($=(I/2F) \cdot t_I$ for constant positive current

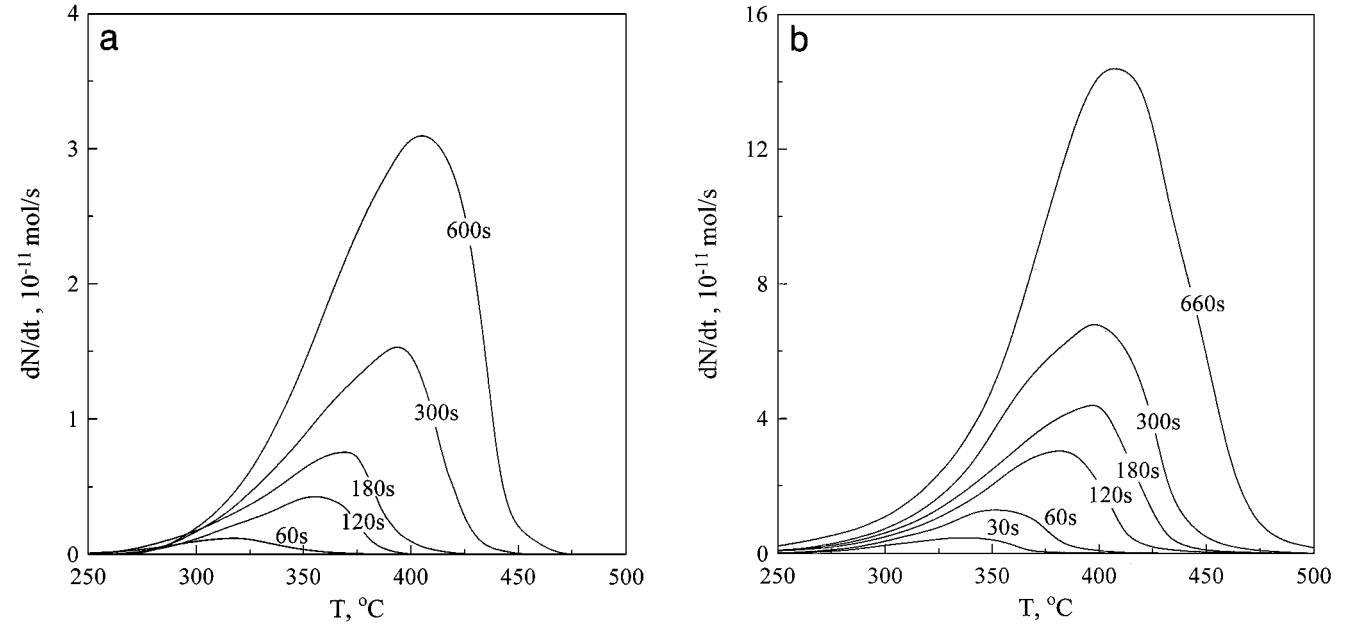

FIG. 9. (a, b) Oxygen thermal desorption spectra after electrochemical O^{2-} supply on the Ag film through the solid electrolyte at 300°C. The different curves correspond to various times of current application: (a) $I = +2\,\mu A$ and (b) $I = +5\,\mu A$. Desorption was performed with a linear heating rate, $\beta = 1$ K/s.

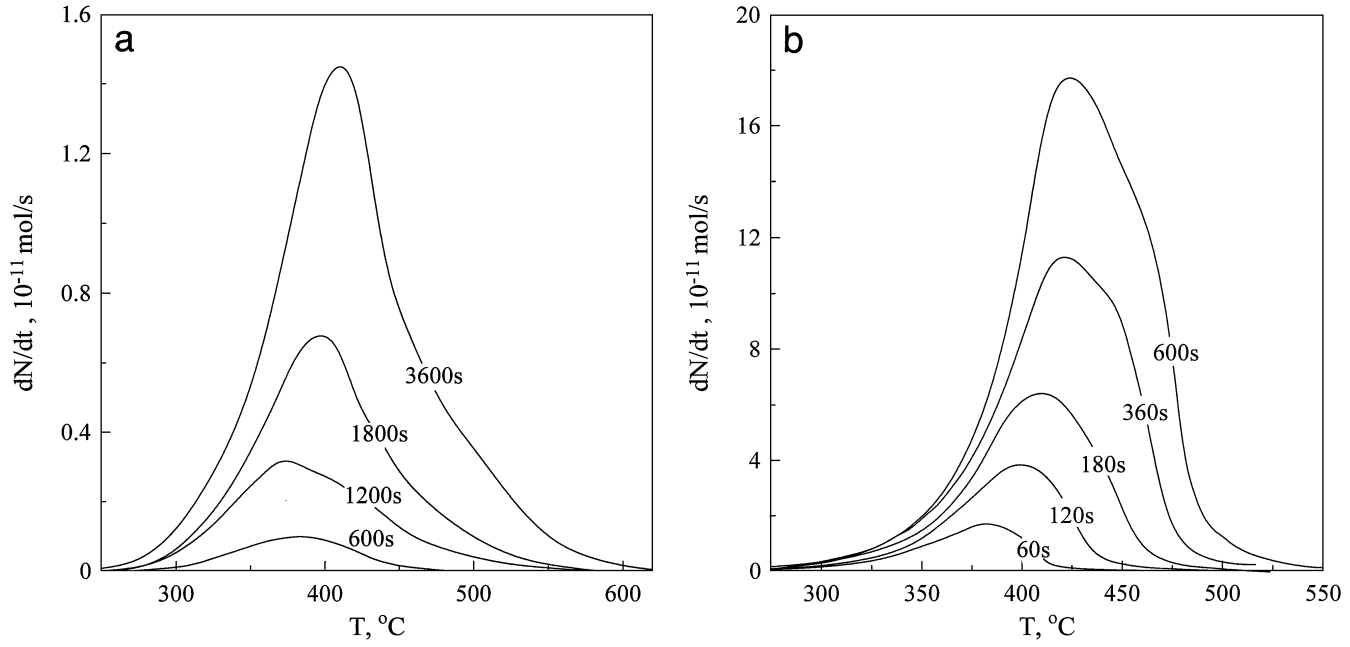

FIG. 10. (a, b) Thermal desorption spectra after electrochemical O^{2-} film supply on the Ag through the solid electrolyte at 350°C. The different curves correspond to various times of current application: (a) $I = +2\ \mu$A and (b) $I = +10\ \mu$A. Desorption was performed with a linear heating rate, $\beta = 1$ K/s.

application). Figure 13 shows the effect of oxygen coverage on the sticking coefficient during electrochemical adsorption under the conditions of Figs. 9b, 10a, and 10b. The main points of this figure are the following:

1. The sticking coefficient is much higher than in gas phase adsorption, reaching a value of 0.75 for $T_{ads} = 300$°C. As expected the lower the adsorption temperature the higher the sticking coefficient.

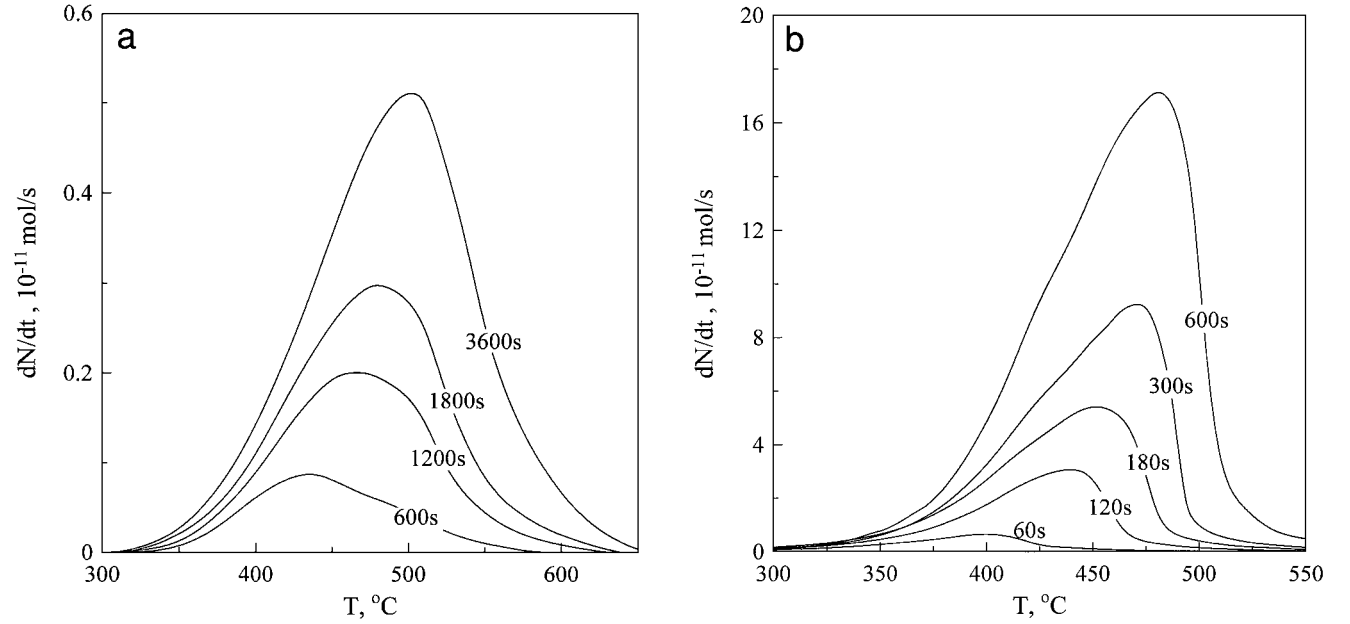

FIG. 11. (a, b) Thermal desorption spectra after electrochemical O^{2-} supply on the Ag film through the solid electrolyte at 400°C. The different curves correspond to various times of current application: (a) $I = +3\ \mu$A and (b) $I = +15\ \mu$A. Desorption was performed with a linear heating rate, $\beta = 1$ K/s.

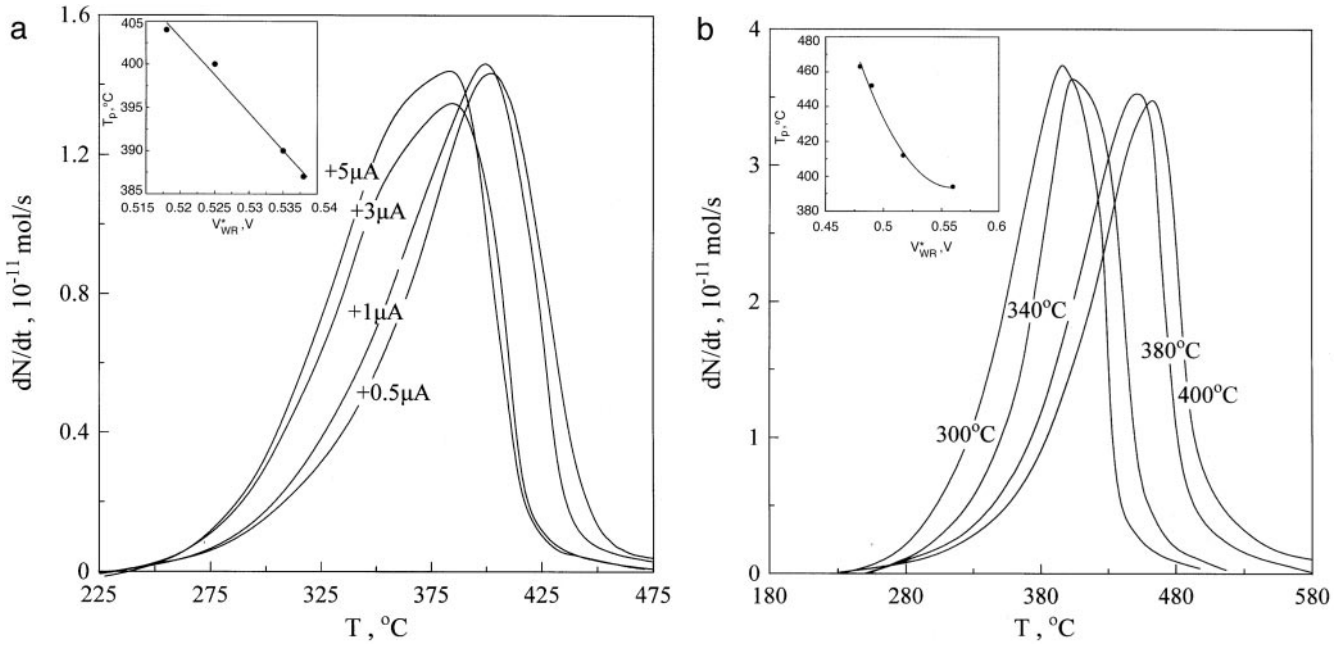

FIG. 12. (a) Thermal desorption spectra after electrochemical O^{2-} supply at 300°C. The different curves correspond to various currents, as indicated on each curve, and to various times of current application in order to achieve almost the same initial coverage. Desorption was performed with linear heating rate, $\beta = 1$ K/s. (Inset) Effect of potential on peak temperature. (b) Thermal desorption spectra after electrochemical O^{2-} supply through the electrolyte for 10 min. Each curve corresponds to different adsorption temperature and current in order to achieve almost the same initial coverage. Desorption was performed with linear heating rate, $\beta = 1$ K/s. (Inset) Effect of potential on peak temperature.

2. As a result of the high values of S, the oxygen coverages are relatively high.

3. S is lower at small coverages and increases as the latter increases reaching a constant value. This may be due to the formation of subsurface oxygen which is favored for higher oxygen coverage.

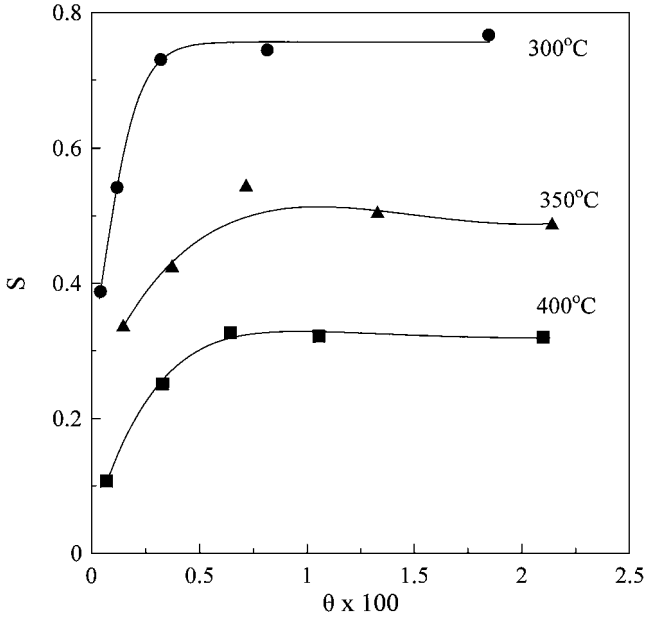

FIG. 13. Sticking coefficient as a function of coverage during electrochemical adsorption corresponding to Figs. 9a, 10b, and 11b.

As described in the experimental section, a series of 56 experiments employing different initially imposed potentials, V^*_{WR}, and different heating rates, β, was performed *at low oxygen coverage* in order to investigate the effect of catalyst potential on peak desorption temperatures. At low coverage only atomic oxygen is formed. A summary of these results is presented in Fig. 14a where the effect of potential on the activation energy of desorption and the preexponential factor is presented. The features of these plots are the same as in the case of Pt (82, 83). First, the activation energy of desorption decreases linearly with increasing potential, with a slope equal to -1, that is $\Delta E_d = e\Delta V_{WR}$. This confirms the hypothesis that the catalyst potential and work function (since $\Delta(e\Phi = e\Delta V_{WR}$ (85, 86)) has a pronounced effect on the binding strength of atomic oxygen as determined in previous TPD investigations (82, 83) and ab initio quantum mechanical calculations using model metal clusters (91). The preexponential factor of desorption (computed from $\nu = \beta \cdot (\frac{E}{RT_p^2}) \cdot \exp(\frac{E}{RT_p})$ for first-order desorption (92)) exhibits a more complex dependence on film potential, since there is a maximum at $V^*_{WR} \approx 0.59$ V. The same qualitative conclusions are reached if one chooses to plot E_d vs the catalyst potential value, $V_{WR,P}$, at the peak desorption temperature (Fig. 14b). The slope of E_d vs $eV_{WR,P}$ is -1.73 and the preexponential factor maximum at $V_{WR,P} \approx 0.53$ V.

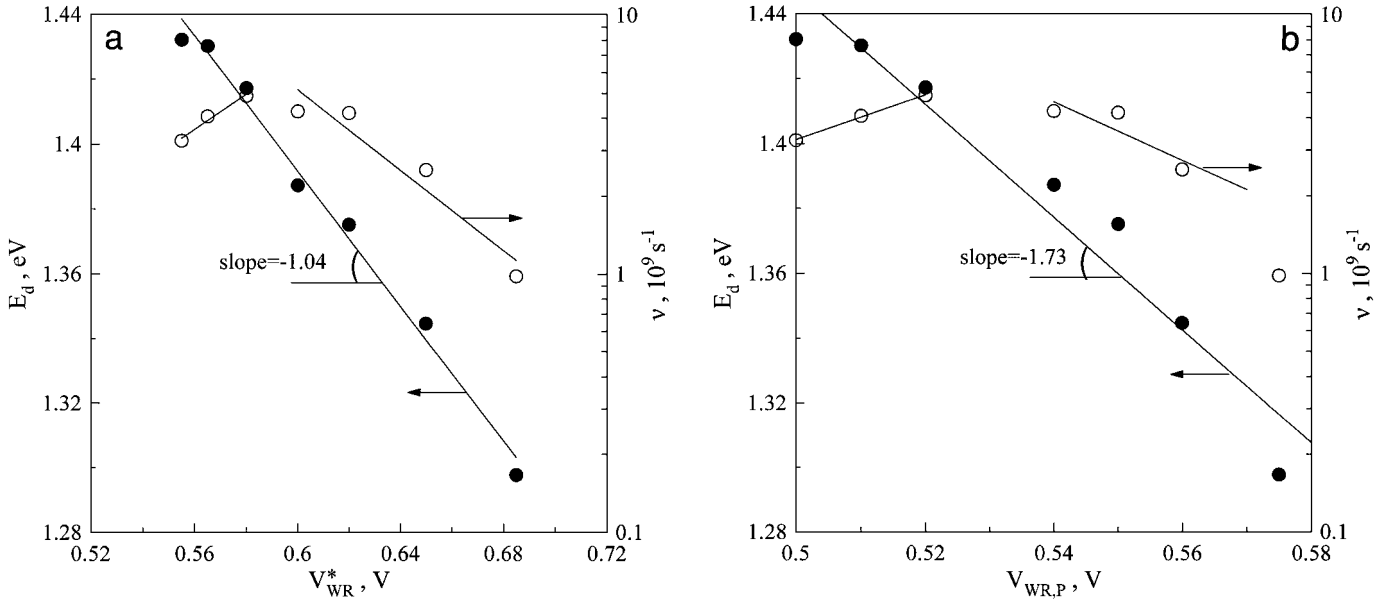

FIG. 14. (a) Effect of catalyst potential, V^*_{WR}, on the desorption activation energy (●), calculated from modified Redhead analysis (88), and on the first-order preexponential factor (○). (b) Effect of catalyst potential at peak desorption temperature, $V_{WR,P}$, on the desorption activation energy (●), calculated from modified Redhead analysis (88), and on the first-order preexponential factor (○).

We believe that the first mode of presentation (E_d vs V^*_{WR}, Fig. 14a) is more meaningful as it relates E_d to the catalyst potential before the adsorbed oxygen layer has been partly destroyed due to desorption.

It is worth noting that, contrary to the case of Pt (82, 83), where the dependence of E_d on V^*_{WR} could be studied over a very wide range (0 to 0.8 eV) in the present case the corresponding, experimentally accessible, V^*_{WR} range is rather narrow (0.52 to 0.68 eV). This is because any finite galvanostatically imposed positive current (O^{2-} supply to the catalyst) was found cause a significant increase in V^*_{WR} to values higher than 0.5 eV. This is also apparent from the cyclic voltammograms discussed below and must be related to the ability of Ag to dissolve significant amounts of oxygen as subsurface oxygen (52, 74) so that a significant overpotential, and correspondingly high V^*_{WR} and work function $e\Phi$ value (54), is necessary to cause oxygen desorption and thus to the sustain a steady-state current. Consequently, extrapolation of the results presented in Figs. 14 to the limit of nonelectrochemical, i.e., gas phase adsorption ($V_{WR} \leq 0$), is not possible, as in the case of Pt (82, 83). As previously noted the E_d for gaseous adsorption was found to be 130–140 kJ/mol, i.e., in the range of 1.35 to 1.45 eV in agreement with literature (9, 25–28, 32, 50).

3. *Mixed Gas and Electrochemical Adsorption*

This mode of operation has been described in the experimental section. The main results are summarized on Figs. 15a and 15b. In this case the formation of two types of oxygen species is clear. As in the case of Pt (82, 83), the high temperature species forms mainly after prolonged current application corresponding to coverages above 0.1. It is worth noting that this state desorbs at temperatures significantly lower than subsurface oxygen and thus must correspond to a surface species. The role of this species on the binding strength of atomic oxygen appears to be similar to that of subsurface oxygen. That is, the chemisorption bond strength of oxygen decreases due to the presence of the strongly bonded "ionic" species. A decrease of the peak temperature of the weakly bonded atomic oxygen is observed from $\sim 380^\circ$C via electrochemical adsorption to $\sim 350^\circ$C via mixed gaseous and electrochemical adsorption.

For the special case of Ag deposited on YSZ, the ethylene epoxidation reaction is enhanced by electrochemical oxygen ion supply to Ag catalyst through the solid electrolyte (73). The observed behavior can be understood within the frame of the electrochemical promotion (EP) or NEMCA effect (56) by taking into account the induced change in the average work function of the catalyst surface as a result of the electrochemically induced spillover of ions onto the catalyst surface (85, 86) and of the concomitant controlled change in the strength of chemisorptive bonds (56, 85, 86). Specifically, spillover oxygen ions cause an increase in catalyst work function and as a result a decrease in the strength of chemisorptive bond of atomic oxygen (electron acceptor) (56, 73, 85, 86). In addition to the formation of spillover ions, upon current application, dissolved subsurface oxygen emerges on the catalyst surface. As mentioned above, subsurface oxygen also causes a decrease in Ag–O bond strength. Consequently, the atomic oxygen on the silver surface becomes more reactive due to the synergetic

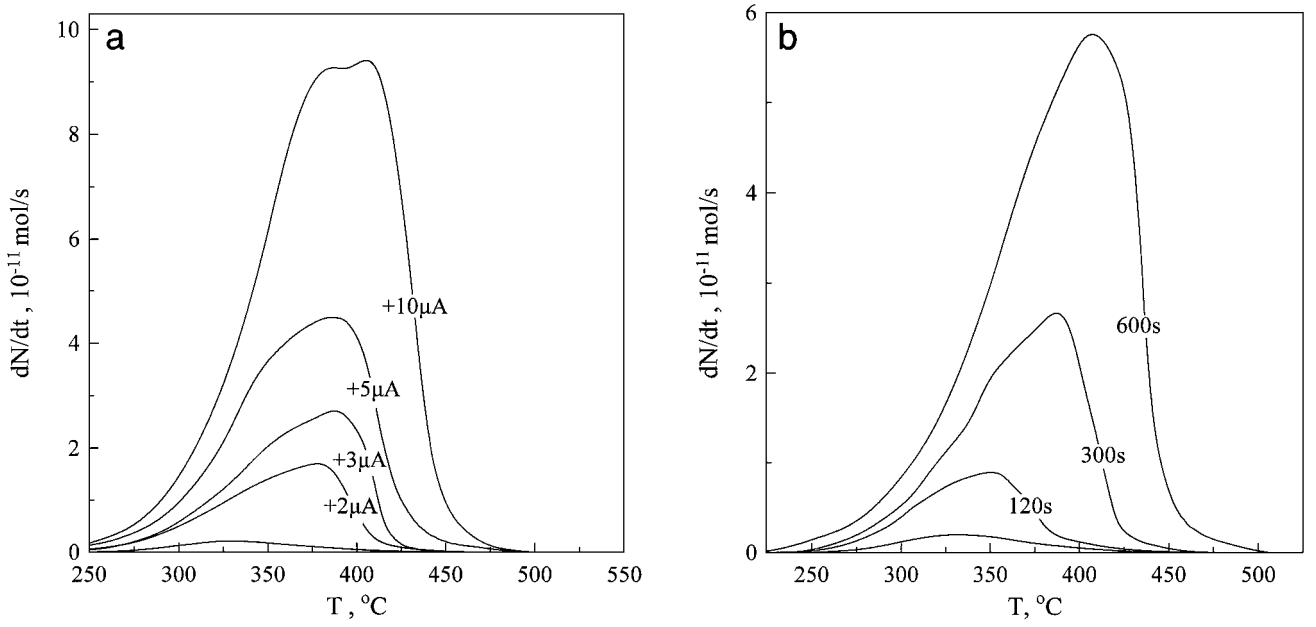

FIG. 15. (a, b) Thermal desorption spectra after gaseous oxygen adsorption at 300°C and an oxygen pressure of 6×10^{-6} Torr for 15 min (5.4 kL) followed by electrochemical O^{2-} supply for (a) 3 min with various currents and (b) various time periods with a constant current of $+2\ \mu$A. Desorption was performed with a linear heating rate, $\beta = 1$ K/s.

action of spillover and subsurface oxygen and thus the rate of ethylene epoxidation reaction is enhanced.

4. *Cyclic Voltammetry*

Figure 16 shows a cyclic voltammogram of the Ag film exposed to ultrahigh vacuum at 350°C. The Ag film potential with respect to the Au reference electrode is varied -2 to $+1.5$ V with a scan rate of 20 mV/s. The different curves of this figure obtained by varying the holding time at $V_{WR} = +1.5$ V, as indicated on each curve. The anodic ($I > 0$) peaks to the right are due to the formation of adsorbed oxygen and the oxygen evolution in the gas phase. The reduction of the two types of adsorbed oxygen is shown

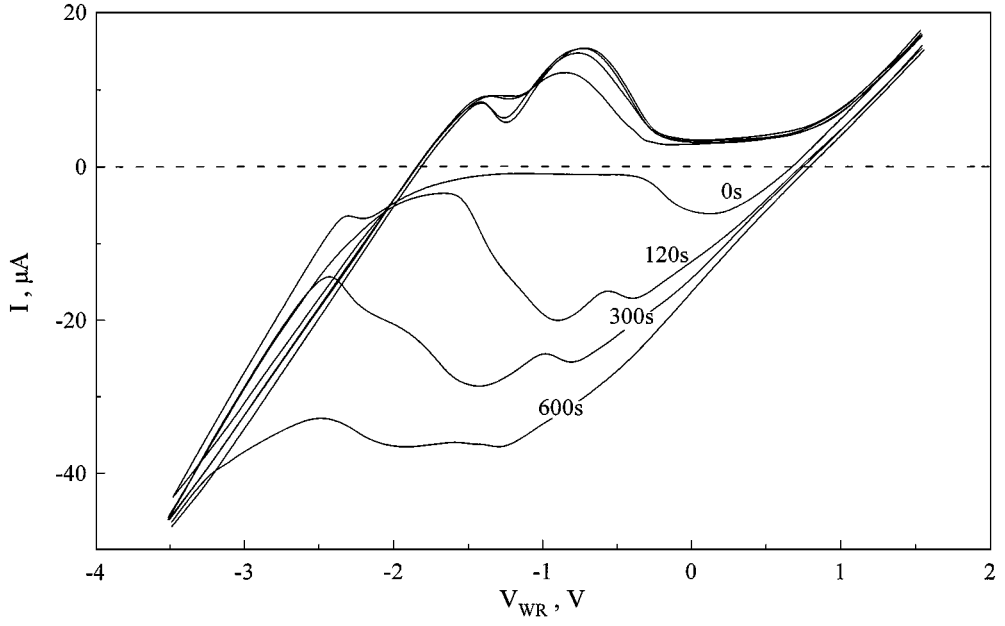

FIG. 16. Cyclic voltammograms of the Ag film at 350°C and various holding times under UHV. Holding potential, 1.5 V; scan rate, 20 mV/s.

clearly at the cathodic part of the voltammograms. They correspond to normally chemisorbed and ionic oxygen species, at high and low potentials, respectively, in agreement with the corresponding TPD spectra. The peak at lower peak potential, ionic oxygen, increases with increasing holding time, while the other peak, normally chemisorbed oxygen, appears almost unaffected. Both peaks are shifted to lower potentials as the holding time increases. It is interesting that the cyclic voltammograms reveal the same qualitative feature about the state of adsorbed oxygen as the corresponding thermal desorption spectra do (Figs. 9–12) but provide a more clear distinction of the two types of oxygen on the Ag catalyst surface.

5. *Comparison of Gaseous, Electrochemical, and Mixed Adsorption*

Figure 17 compares oxygen TPD spectra obtained with the three different modes of adsorption, gaseous, electrochemical, and mixed, under the same conditions. In all three cases the adsorption temperature, T_{ads}, was 300°C, the oxygen exposure (for gaseous and mixed adsorption) 5.4 kL, and the amount of electrochemically supplied oxygen (for electrochemical and mixed adsorption) 4.6×10^{-9} mol O (i.e., 5 μA for 180 s).

Consequently this figure can serve as a basis of interpreting the effect of electrochemical promotion, or NEMCA, when using positive currents and potentials with Ag catalysts deposited on YSZ. To this end one must compare the TPD spectra for gaseous and mixed adsorption (Fig. 17) which correspond to the open-circuit and electrically biased (NEMCA) states of a Ag catalyst during catalytic oxidations.

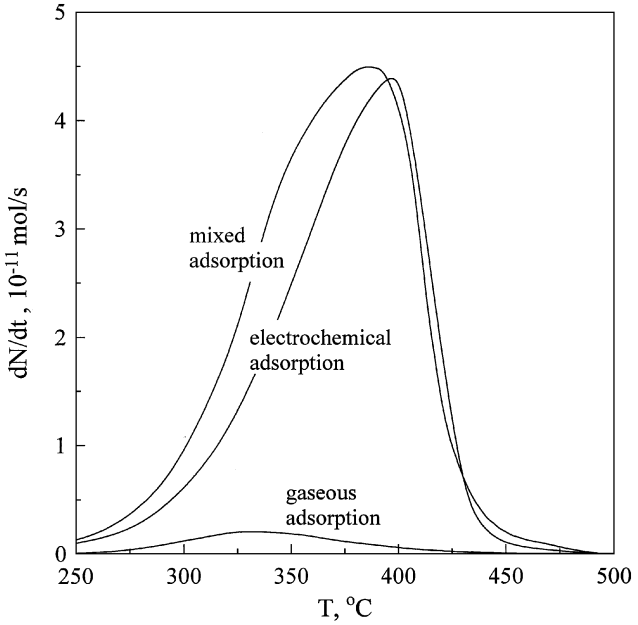

FIG. 17. Comparison of the oxygen TPD spectra obtained with the three different modes of adsorption, gaseous, electrochemical, and mixed, under the same conditions: $T_{ads} = 300$°C, 5.4 kL of oxygen exposure (for gaseous and mixed adsorption), and 4.6×10^{-9} mol O of electrochemically supplied oxygen (for electrochemical and mixed adsorption), i.e., 5 μA for 180 s.

Two main observations can be made:

1. Mixed adsorption leads to much higher oxygen coverages than gaseous adsorption. Thus the amount of oxygen desorbing at the gaseous peak desorption temperature ($T_p = 330$°C) is a factor of 10 higher during mixed adsorption. This observation by itself provides a means of rationalizing the NEMCA effect with Ag/YSZ.

2. Mixed adsorption leads to the creation of two adsorption states although the separation is not as clear as in the case of Pt. The strongly bonded state ($T_p \approx 380$–400°C) is identical to the one formed via electrochemical adsorption (Fig. 17). As in the case of Pt (82, 83), this state can act as a sacrificial promoter during NEMCA experiments of catalytic oxidations; i.e., it promotes the rate of the reaction by increasing V^*_{WR} (and $e\Phi$) and thus weakening the chemisorptive bond of the more weakly bonded state (Fig. 14) but at the same time is consumed by the hydrocarbon at a rate Λ times lower than the more weakly bonded state (56). Its rate of consumption (thereby "sacrificial" promoter) equals at steady state in NEMCA experiments its rate of formation $I/2F$. The weakly bonded state ($T_p \approx 340$°C) desorbs approximately at the same temperature with the gaseous adsorption state. This is different from the case of Pt where the weakly bonded state was found to desorb at temperatures 50°C lower than the gaseous adsorption state (82, 83). This can explain the much higher rate enhancement ratio, ρ, values obtained with electrochemical promotion on Pt vs Ag for oxidation reactions (e.g., $\rho \approx 60$ for C_2H_4 oxidation on Pt (93) and $\rho \approx 3$ for C_2H_4 oxidation on Ag (74, 75)).

CONCLUSIONS

The main conclusions from the present study are the following:

1. Subsurface oxygen formation takes place for adsorption temperatures above 350°C.

2. Electrochemical O^{2-} pumping to the Ag catalyst causes backspillover of large amounts of oxygen on the catalyst surface and leads to the formation of two oxygen adsorption states, i.e, a strongly bonded anionic oxygen along with the weakly bound atomic oxygen. The two oxygen species coexist on the surface.

3. The strongly bonded backspillover oxygen species does not form via adsorption from the gas phase. It is formed only electrochemically and can act as a sacrificial promoter during catalytic oxidations.

4. The desorption activation energy of oxygen decreases linearly with increasing catalyst potential. This decrease

implies a pronounced increase in the desorption rate of adsorbed oxygen at any fixed temperature and thus an increase in the reactivity of adsorbed oxygen for catalytic oxidation reactions.

The present results provide an explanation for the electrochemical promotion behavior of Ag catalysts deposited on oxygen-ion conductors. The underlying promotional mechanism bears several similarities with the case of Pt (82) and stems from the observation that solid state electrochemistry can induce new types of oxygen adsorption on Ag surfaces interfaced with solid electrolytes.

ACKNOWLEDGMENTS

We thank EPRI and Du Pont for partial financial support and our reviewers for several useful comments.

REFERENCES

1. Campbell, C. T., and Paffett, M. T., *Surf. Sci.* **139**, 396 (1984).
2. Voge, H. H., and Adams, C . R., *Adv. Catal.* **17**, 151 (1967).
3. Sachtler, W. M. H., *Catal. Rev.* **4**, 27 (1970).
4. Sachtler, W. M. H., Backx, C., and van Santen, R. A., *Catal. Rev.* **23**, 127 (1981).
5. Kleyn, A. W., Butler, D . A., and Raukema, A., *Surf. Sci.* **363**, 29 (1996).
6. Besenbacher, F., and Nørskov, J. K., *Prog. Surf. Sci.* **44**, 1 (1993).
7. van der Hoek, P. J., and Baerends, E. J., *Surf. Sci.* **221**, L791 (1989).
8. Nakatsuji, H., and Nakai, H., *Chem. Phys. Lett.* **174**, 283 (1990).
9. Engelhardt, H. A., and Menzel, D., *Surf. Sci.* **57**, 591 (1976).
10. Albers, H., van der Waland, W. J. J., and Bootsma, G. A., *Surf. Sci.* **68**, 47 (1977).
11. Felter, T. E., Weinberg, W. H., Ya Lastushkina, G., Boronin, A. I., Zhdan, P. A., Boreskov, G. K., and Hrbek, J., *Surf. Sci.* **118**, 369 (1982).
12. Barteau, M. A., and Madix, R. J., *in* "The Chemical Physics of Solid Surfaces and Heterogeneous Catalysis" (D. A. King and D. P. Woodruff, Eds.), Vol. 4, Chap. 4, Elsevier, Amsterdam, 1982.
13. Prince, K. C., Paolucci, G., Bradshaw, A. M., and Horn, K., *Vacuum* **33**, 867 (1983).
14. Campbell, C. T., and Paffett, M. T., *Surf. Sci.* **143**, 517 (1984).
15. Barteau, M. T., and Madix, R. J., *Surf. Sci.* **97**, 101 (1980).
16. Backx, C., de Groot, C. P. M., and Biloen, P., *Appl. Surf. Sci.* **6**, 256 (1980).
17. Backx, C., de Groot, C. P. M., and Biloen, P., *Appl. Surf. Sci.* **104**, 300 (1980).
18. Prince, K. C., and Bradshaw, A. M., *Surf. Sci.* **126**, 49 (1983).
19. Temkin, M. I., *Advan. Catalysis* **28**, 173 (1979).
20. Haul, R., Hoge, D., Neubauer, G., and Zeeck, U., *Surf. Sci.* **122**, L622 (1982).
21. Rao, C. N. R., Vishnu Kamath, P., and Yashonath, S., *Chem. Phys. Lett.* **88**, 13 (1982).
22. Sexton, B. A., and Madix, R. J., *Chem. Phys. Lett.* **76**, 294 (1980).
23. Rovida, G., and Pratesi, F., *Surf. Sci.* **52**, 542 (1975).
24. Vattuone, L., Rocca, M., Boragno, C., and Valbusa, U., *J. Chem. Phys.* **101**, 726 (1994).
25. Rovida, G., *J. Phys. Chem.* **80**, 150 (1976).
26. Bowker, M., Barteau, M. A., and Madix, R. J., *Surf. Sci.* **92**, 528 (1980).
27. Campbell, C. T., *Surf. Sci.* **157**, 46 (1985).
28. Rovida, G., Pratesi, F., Maglietta, M., and Ferroni, E., *Surf. Sci.* **43**, 230 (1974).
29. Campbell, C. T., *Surf. Sci.* **173**, L641 (1986).
30. Benndorf, C., Franck, M., and Thieme, F., *Surf. Sci.* **128**, 417 (1983).
31. Czanderna, A. W., Frank, O., and Schmidt, W. A., *Surf. Sci.* **38**, 129 (1973).
32. Grant, R. B., and Lambert, R. M., *Surf. Sci.* **146**, 256 (1984).
33. Spruit, M. E. M., and Kleyn, A. W., *Chem. Phys. Lett.* **159**, 342 (1988).
34. Buatier de Mongeot, F., Valbusa, U., and Rocca, M., *Surf. Sci.* **339**, 291 (1995).
35. Peuckert, M., *Surf. Sci.* **146**, 329 (1984).
36. Belyaeva, M. E., *Sov. Electrochem.* **24**, 1258 (1988).
37. Hall, P. G., and King, D. A., *Surf. Sci.* **36**, 810 (1973).
38. Kummer, J. T., *J. Phys. Chem.* **63**, 460 (1959).
39. Buttner, F. H., Funk, E. R., and Udin, H., *J. Phys. Chem.* **56**, 657 (1951).
40. Bagg, J., and Bruce, L., *J. Catal.* **2**, 92 (1963).
41. Czanderna, A. W., *J. Phys. Chem.* **68**, 2765 (1964).
42. Czanderna, A. W., *J. Phys. Chem.* **70**, 2120 (1966).
43. McDonald, W. R., and Hayes, K. E., *J. Catal.* **18**, 115 (1970).
44. Janssen, M. M. P., Moolhuysen, J., and Sachtler, W. M. H., *Surf. Sci.* **33**, 624 (1972).
45. Wood, J., *J. Phys. Chem.* **75**, 2186 (1971).
46. Kollen, W., and Czanderna, A. W., *J. Colloid Interface Sci.* **38**, 152 (1972).
47. Joyner, R. W., and Roberts, M. W., *Chem. Phys. Lett.* **60**, 459 (1979).
48. Dean, M., and Bowker, M., *J. Catal.* **115**, 138 (1989).
49. Dean, M., McKee, A., and Bowker, M., *Surf. Sci.* **211/212**, 1061 (1989).
50. Kitson, M., and Lambert, R. M., *Surf. Sci.* **109**, 60 (1981).
51. Arakawa, T., Saito, A., and Shiokawa, J., *Appl. Surf. Sci.* **16**, 365 (1983).
52. van den Hoek, P. J., Baerends, E. J., and van Santen, R. A., *J. Phys. Chem.* **96**, 6469 (1989).
53. Vayenas, C. G., Bebelis, S., and Neophytides, S., *J. Phys. Chem.* **92**, 5083 (1988).
54. Vayenas, C. G., Bebelis, S., and Ladas, S., *Nature (London)* **343**, 625 (1990).
55. Vayenas, C. G., Bebelis, S., Yentekakis, I. V., and Lintz, H.-G., *Catal. Today* **11**, 303 (1992).
56. Vayenas, C. G., Jaksic, M. M., Bebelis, S., and Neophytides, S., *in* "Modern Aspects of Electrochemistry" (J. O'M. Bockris, B. E. Conway, and R. E. White, Eds.), No. 29, pp. 57–202. Plenum Press, New York, 1996.
57. Politova, T. I., Sobyanin, V. A., and Belyaev, V. D., *React. Kinet. Catal. Lett.* **41**, 321 (1990).
58. Basini, L., Cavalca, C. A., and Haller, G. L., *J. Phys. Chem.* **88**, 10853 (1994).
59. Harkness, I., and Lambert, R. M., *J. Catal.* **152**, 211 (1995).
60. Chiang, P. C., Eng, D., and Stoukides, M., *J. Catal.* **139**, 683 (1993).
61. Varkaraki, E., Nicole, J., Plattner, E., Comninellis, Ch., and Vayenas, C. G., *J. Appl. Electrochem.* **25**, 978 (1995).
62. Cavalca, C., and Haller, G. L., *J. Catal.* **177**, 389 (1998).
63. Palermo, A., Tikhov, M. S., Filkin, N. C., Lambert, R. M., Yentekakis, I. V., and Vayenas, C. G., *Stud. Surf. Sci. Catal.* **101**, 513 (1996).
64. Cavalca, A., Larsen, G., Vayenas, C. G., and Haller, G. L., *J. Phys. Chem.* **97**, 6115 (1993).
65. Pliangos, C., Yentekakis, I. V., Ladas, S., and Vayenas, C. G., *J. Catal.* **159**, 189 (1996).
66. Neophytides, S. G., Tsiplakides, D., Stonehart, P., Jaksic, M. M., and Vayenas, C. G., *Nature (London)* **370**, 45 (1994).
67. Grzybowska-Swierkosz, B., and Haber, J., *in* "Annual Reports on the Progress of Chemistry," Vol. 91, pp. 395–439. The Royal Society of Chemistry, Cambridge, 1994.
68. Pritchard, J., *Nature (London)* **343**, 592 (1990).
69. Bockris, J. O'M., and Minevski, Z. S., *Electrochim. Acta* **39**, 1471 (1994).
70. Karavasilis, Ch., Bebelis, S., and Vayenas, C. G., *Mater. Sci. Forum* **76**, 175 (1991).
71. Stoukides, M., and Vayenas, C. G., *J. Catal.* **64**, 18 (1980); **70**, 137 (1981).
72. Stoukides, M., and Vayenas, C. G., *J. Electrochem. Soc.* **131**, 839 (1984).

73. Bebelis, S., and Vayenas, C. G., *J. Catal.* **138**, 588 (1992).
74. Bebelis, S., and Vayenas, C. G., *J. Catal.* **138**, 570 (1992).
75. Karavasilis, Ch., Bebelis, S., and Vayenas, C. G., *J. Catal.* **160**, 190 (1996).
76. Neophytides, S., and Vayenas, C. G., *J. Catal.* **118**, 147 (1989).
77. Tsiakaras, P., and Vayenas, C. G., *J. Catal.* **144**, 333 (1993).
78. Makri, M., Vayenas, C. G., Bebelis, S., Besocke, K. H., and Cavalca, C., *Surf. Sci.* **369**, 351 (1996).
79. Ladas, S., Kennou, S., Bebelis, S., and Vayenas, C. G., *J. Phys. Chem.* **97**, 8845 (1993).
80. Basini, L., Cavalca, C. A., and Haller, G. L., *J. Phys. Chem.* **88**, 10853 (1994).
81. Kondarides, D. I., Papatheodorou, G. N., Vayenas, C. G., and Verykios, X. E., *Ber. Bunsenges Phys. Chem.* **97**, 709 (1993).
82. Neophytides, S. G., Tsiplakides, D., and Vayenas, C. G., *J. Catal.* **178**, 414 (1998).
83. Neophytides, S. G., and Vayenas, C. G., *J. Phys. Chem.* **99**, 17063 (1995).
84. Zipprich, W., Wiemhöfer, H.-D., Vöhrer, U., and Göpel, W., *Ber. Bunsengesel. Phys. Chem.* **99**, 1406 (1995).
85. Vayenas, C. G., Bebelis, S., and Ladas, S., *Nature (London)* **343**, 625 (1990).
86. Ladas, S., Bebelis, S., and Vayenas, C. G., *Surf. Sci.* **251/252**, 1062 (1991).
87. Nicole, J., Tsiplakides, D., Wodiunig, S., and Comninellis, Ch., *J. Electrochem. Soc.* **L312**, 144 (1997).
88. Falconer, J. L., and Madix, R. J., *Surf. Sci.* **48**, 393 (1975).
89. Falconer, J. L., and Madix, R. J., *J. Catal.* **48**, 262 (1977).
90. Neophytides, S. G., Tsiplakides, D., and Vayenas, C. G., in preparation.
91. Pacchioni, S., Ilas, F., Neophytides, S., and Vayenas, C. G., *J. Phys. Chem.* **100**, 16653 (1996).
92. Habenschaden, E., and Küppers, J., *Surf. Sci.* **138**, L147 (1984).
93. Bebelis, S., and Vayenas, C. G., *J. Catal.* **118**, 125 (1989).